The University of Nottingham
UNITED KINGDOM · CHINA · MALAYSIA

Mitchell-Smith, Jonathon and Speidel, Alistair and Clare, A.T. (2018) Transitory electrochemical masking for precision jet processing techniques. Journal of Manufacturing Processes, 31 . pp. 273-285. ISSN 1878-6642

Access from the University of Nottingham repository:
http://eprints.nottingham.ac.uk/48532/1/1-s2.0-S1526612517303638-main.pdf

Copyright and reuse:

The Nottingham ePrints service makes this work by researchers of the University of Nottingham available open access under the following conditions.

This article is made available under the University of Nottingham End User licence and may be reused according to the conditions of the licence. For more details see: http://eprints.nottingham.ac.uk/end_user_agreement.pdf

A note on versions:

The version presented here may differ from the published version or from the version of record. If you wish to cite this item you are advised to consult the publisher's version. Please see the repository url above for details on accessing the published version and note that access may require a subscription.

For more information, please contact eprints@nottingham.ac.uk

Journal of Manufacturing Processes 31 (2018) 273–285

Contents lists available at ScienceDirect

Journal of Manufacturing Processes

journal homepage: www.elsevier.com/locate/manpro

Transitory electrochemical masking for precision jet processing techniques

J. Mitchell-Smith, A. Speidel, A.T. Clare*

Advanced Component Engineering Laboratory (ACEL), Advanced Manufacturing Technology Group, University of Nottingham, Nottingham, NG7 2RD, United Kingdom

ARTICLE INFO

Article history:
Received 1 October 2017
Received in revised form
23 November 2017
Accepted 26 November 2017

Keywords:
Electrolyte doping
Electrochemical machining
Electrolyte jet machining
Ecm
Electrochemical jet processing
Nickel superalloy

ABSTRACT

Electrochemical jet processing techniques provide an efficient method for large area surface structuring and micro-milling, where the metallurgy of the near-surface is assured and not adversely affected by thermal loading. Here, doped electrolytes are specifically developed for jet techniques to exploit the Gaussian energy distribution as found in energy beam processes. This allows up to 26% reduction in dissolution kerf and enhancements of the defined precision metric of up to 284% when compared to standard electrolytes. This is achieved through the filtering of low energy at discrete points within the energy distribution curve. Two fundamental mechanisms of current filtering and refresh rate are proposed and investigated in order to underpin the performance enhancements found using this methodology. This study aims to demonstrate that a step change in process fidelity and flexibility can be achieved through optimisation of the electrochemistry specific to jet processes.

© 2017 Published by Elsevier Ltd on behalf of The Society of Manufacturing Engineers.

1. Introduction

It is widely recognised that component surface enhancement through the application of multiple scale surface structures is paramount to the optimisation of a component's performance [1–5]. Realisation of these complex, often biologically inspired surfaces presents a significant manufacturing challenge. Electrochemical methods present distinct advantages over more commonly used technologies [6–9]. Creation of highly complex surfaces over a large area, while preserving the metallurgy of the near-surface is not easily achieved. Conventional processes which rely on thermal or shear-based interaction with a tool or energy beam can impart detrimental surface effects, such as residual stress and thermally affected zones.

Electrolyte jet processing (EJP) is a high-precision variant of electrochemical machining (ECM). EJP is the amalgamation of electrochemical jet machining (EJM) [10] and electrochemical jet deposition (EJD) [11,12] within a unified machine tool [13]. An electrolytic cell is formed between the nozzle, and the workpiece confined within the electrolyte jet (see Fig. 1). At sufficient velocity, a thin film area develops radially about the nozzle as the jet impinges. This creates a high resistance area on the target surface, which restricts current allowing for mask-less deposition or removal of material. In most experimental apparatus, this is further aided by an air shroud, co-axial to the nozzle (Fig. 1a) helping to constrict the jet further and also serving to assist in debris and gas bubble removal which form during machining [14].

EJP in subtractive mode has been successfully applied in creating *meso*- and micro-scale surface structures across a wide range of materials [15–21] and applications [22–26]. Prior research work has been carried out to enhance EJP through modification to the nozzle tip [13], enabling modulation of the machined profile, which is distinct from that resulting due to the Gaussian energy distribution (Fig. 1b and c). This modulation of the resistance in-jet allows the response geometry to achieve not only application specific features but, enhanced dimensional accuracy. This is manifested by reduced side wall taper and flatter cut floors analogous to more conventional machining methods.

Electrolyte feedstocks have been investigated in order to enhance resultant finish in EJP [27]. However, electrochemistry within the inter-electrode gap (IEG) has not been a design criterion in previous studies.

1.1. Profile fidelity enhancements

The electrolyte itself has a significant effect on the precision of feature creation due to characteristic conductivity profile specific to each electrolyte [28]. The concentration and composition of elec-

* Corresponding author.
E-mail address: adam.clare@nottingham.ac.uk (A.T. Clare).

https://doi.org/10.1016/j.jmapro.2017.11.028
1526-6125/© 2017 Published by Elsevier Ltd on behalf of The Society of Manufacturing Engineers.

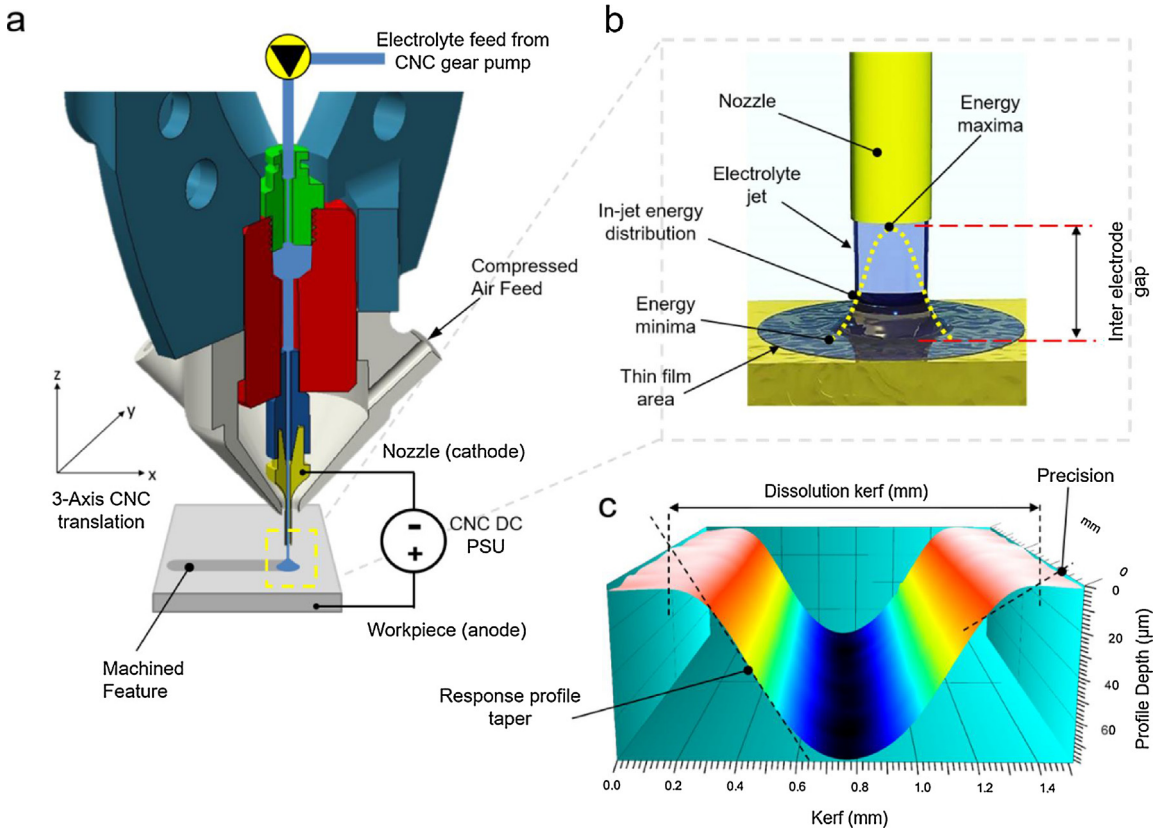

Fig. 1. (a) Schematic showing the rudimentary configuration of EJP apparatus in the subtractive mode (b) detailed schematic of jet interaction zone demonstrating Gaussian energy distribution in-jet (c) extracted resultant machined profile with geometrical definitions.

trolytes used in ECM and EJP specifically have been demonstrated [27,29] to influence the stochastic morphology of the machined surfaces. Electrolyte current efficiency dominates the fidelity of electrochemical machining processes [30,31]. This can be modulated for a given solution by controlling current density. Previous contributions in this field [17] have highlighted the role played by the electrolyte in defining process precision.

The relationship between current density and current efficiency is exaggerated for EJP techniques due to large spatial current density differentials [32]. This causes localised regions where current density exceeds the well-understood activation threshold and thus the onset of machining. Rounded profile features and significant side wall taper (Fig. 1c) are observed [33,34] due to the extremes in current density found across the jet when using conventional ($NaNO_3$ and NaCl) electrolytes. This is problematic since material removal/deposition rate is proportional to current density.

The effect of electrolyte composition has been reported to affect dimensional accuracy in the more established practice of electrochemical machining (ECM). The type of electrolyte to be used has been investigated [35,36] alongside concentration [31,37], which have been shown to improve precision. However, these innovations, although effective in general ECM, are not so applicable to EJP. This being due to the aforementioned large spatial current density differentials across the jet diameter.

Previous attempts to negate this deleterious effect and therefore improve the dimensional accuracy and aspect ratio of the deterministic feature have included the innovation of the hybrid EJM processes. Laser-assisted EJM [38–41] has been employed as a 'focussing' tool to enhance the conductivity at the centre of the electrolyte jet, through a localised temperature increase. This serves to normalise the effective current density outside of the central machining region to reduce overcut. Electrochemical slurry-jet machining [42,43] was developed, whereby the anodic dissolution mechanism is complemented by the application of abrasive jet, again increasing the material removal rate leading to higher aspect ratio holes, although at the loss of surface quality. A further adaptation is the introduction of a pulsed current power supply. First exploited in general electrochemical machining [37,44,45] inhomogeneity in the flow field is reduced due to the rapid updating of the electrolyte. This ensures that machining is restricted to beneath the jet as the electric double layer takes longer to form in the lower current density areas at the periphery of the jet [46,47].

It is hypothesised that significant process enhancements can be achieved by exploiting in-jet electrochemical reactions through doping of conventional electrolytes. It is proposed that when coupled with modified nozzles, predefined and high-fidelity profile geometries can be created. This study aims to demonstrate that a step change in process fidelity and flexibility can be achieved through optimisation of the electrochemistry specific to jet processes.

1.2. Current efficiency

Electrolytes such as $NaNO_3$ and NaCl are commonly employed in electrochemical jet techniques due to their low cost, availability and comparatively low toxicity. Despite response being dependent upon work piece material, these can lead to significantly different resultant profiles. Aggressive electrolytes such as chloride are understood to maintain high current efficiency over a wide range of current densities [28]. In comparison, the current efficiency when machining with sodium nitrate increases with current density, within current density ranges used in EJP. Noting the typical Gaussian distribution of current density found when a standard cylindrical nozzle is used (Fig. 1b). This can lead to significant mate-

Table 1
Nominal composition of Inconel 718% wt, including an inferred ECE in order to calculate theoretical material removal rates.

	Ni	Cr	Nb	Mo	Ti	Al	Co	Si	Mn	Cu	C	P	Fe
% wt.	53.4	18.8	5.27	2.99	1.02	0.50	0.17	0.12	0.07	0.07	0.03	0.01	Bal
ECE (kg/C)	0.304	0.180	0.019	0.025	0.124	0.093	0.031	0.073	0.285	0.659	0.018	0.006	0.019

rial removal occurring outside of the intended machining area, leading to the overcut phenomenon, or so called secondary machining [13].

Evaluating the experimental volume of material removal across a range of current densities allows comparison to the theoretical maximum removal obtained through Faraday's law. Thus giving, η, the current efficiency for a particular electrolyte solution (Eq. (1)).

$$\eta = \frac{M}{\left(\frac{A}{zF}\right) I} \quad (1)$$

Where M is the experimentally observed mass removal, A, the incident surface area, z the assumed dissolution valence, F the Faraday constant and I the current.

Secondary machining zones are observed in EJP at the periphery of the jet where current density is lowest. In order to enhance the precision of the process it is desirable to elevate the activation current density for the electrolyte to enable work piece dissolution.

Iodide would not usually present itself as a viable alternative to nitrate and chloride electrolytes due to the higher cost and negligible increase in conductivity over comparable solutions. However, it is proposed that the characteristic ease of oxidation of iodide to molecular iodine, to form an anodic film, could create a transitory current filter when an electrical potential is applied. It is proposed that the evolution of the anodic film would require an energy transfer resulting in reduced current available to invoke machining. This could negate some of the deleterious effects observed when using other common electrolytes in low current density regions.

2. Methodology

2.1. Experimental apparatus

Experimentation was carried using a previously developed CNC EJP platform built by the investigators [18]. The apparatus consists of a stainless-steel nozzle supplying the electrolyte jet acting as the cathode. This is coupled to the workpiece (anode) via a CNC PSU which is enabled to fix current whilst allowing potential difference to float to meet the desired demand. The electrolyte is supplied from a reservoir using a Diener precision gear pumps. Both PSU and electrolyte supply pump are controlled by the main machine CPU which also controls the 3-axis motion to translate the jet across the workpiece. Toolpath, nozzle traverse speed, electrolyte selection and flow rate, which pertains to electrolyte jet velocity and applied current, can be controlled dynamically and as part of a central control code.

2.2. Material considerations

A Ni-super-alloy, Inconel 718, was used as the workpiece for all experiments. This workpiece was chosen for its poor conventional machinability (American Iron and Steel Institute (AISI) machinability rating 0.3 compared to B1112 grade Steel machinability rating of 1). It is commonly used in high-value manufacturing components where high-temperature mechanical properties are sought. Previous work has demonstrated the sensitivity of this material to current density modulation and the effect on the resultant surface finish [18]. Nominal material composition is outlined in Table 1 accompanied by the weighted average inferred electrochemical equivalent (ECE) at a fixed current density. All samples were pre-polished to ≈ 1 μm surface roughness (R_a) before machining. Samples were cleaned post-process in an ultrasonic bath and swabbed with acetone before microscopic inspection.

Throughout these experiments, and for simplification, the doped electrolytes will be referred to as NaI, with the corresponding percentage (of the ionic strength), of the sodium iodide component following it, as shown in Table 2. $NaNO_3$ and NaI are combined in the in dry salt form to the required ratio by weight and deionised water added dissolving the salts to form the electrolyte.

During surface processing demonstrations and comparison of modified nozzle profiles the electrolyte velocity was maintained at a constant of 16 m/s (1 mm, 0.5 mm and 0.25 mm I.D nozzles) (Fig. 10–12) to match the maximum possible jet speed achievable by the system when using a 1 mm I.D. nozzle. For the refresh rate experimentation, detailed later, jet speed was varied from 4 m/s to 29 m/s (the upper and lower bounds of machine capability with a 0.5 mm I.D. nozzle). In all other cases, the electrolyte velocity was maintained at 25 m/s being an arbitrary value used generally during processing with a 0.5 mm I.D. nozzle. The inter electrode gap (IEG) was set initially through an automated touch-sense system [19] at 0.25 mm for the modified and 1 mm I.D. nozzle and 0.5 mm in all other cases. For surface structuring a constant applied current of 900 mA ($J = 100$ A/cm^2) for 1 mm nozzle, 900 mA ($J = 400$ A/cm^2) for the 0.5 mm nozzle and 200 mA ($J = 400$ A/cm^2) for 0.25 mm nozzle. Where J is the predicted mean current density at the nozzle. In the case of the electrolyte efficiency test current density ranged from 20 A/cm^2 to 200 A/cm^2. The refresh rate and incident iodide concentration were both appraised at 100 A/cm^2. The electrical potential was left to float as this was seen to vary dependant on the nozzle geometry, electrolyte conductivity, and surface geometry, and therefore subsequent resistance. Where nozzle translation was

Table 2
Electrolyte composition and conductivity for the range of concentrations used within this study. All measurements taken at 23 °C (SD 0.2 °C).

Electrolyte	Component Composition Ratio (M)	Overall Electrolyte Ionic Strength and Molar Concentration (M)	Electrolyte Conductivity (ms/cm^{-1})
NaCl	2.3: 0	2.3	165.4 (SD 0.1%)
$NaNO_3$	2.3: 0	2.3	136.6 (SD 0.03%)
$NaNO_3$	1.8: 0	1.8	116 (SD 0.1%)
$NaNO_3$ + 5% NaI (*NaI5*)	2.185: 0.115	2.3	137.7 (SD 0.1%)
$NaNO_3$ + 10% NaI (*NaI10*)	2.07: 0.23	2.3	139.7 (SD 0.1%)
$NaNO_3$ + 15% NaI (*NaI15*)	1.955: 0.345	2.3	141.8 (SD 0.1%)
$NaNO_3$ + 20% NaI (*NaI20*)	1.84: 0.46	2.3	143.3 (SD 0.2%)
$NaNO_3$ + 30% NaI (*NaI30*)	1.61: 0.69	2.3	145.6 (SD 0.1%)
$NaNO_3$ + 40% NaI (*NaI40*)	1.38: 0.92	2.3	149.4 (SD 0.1%)

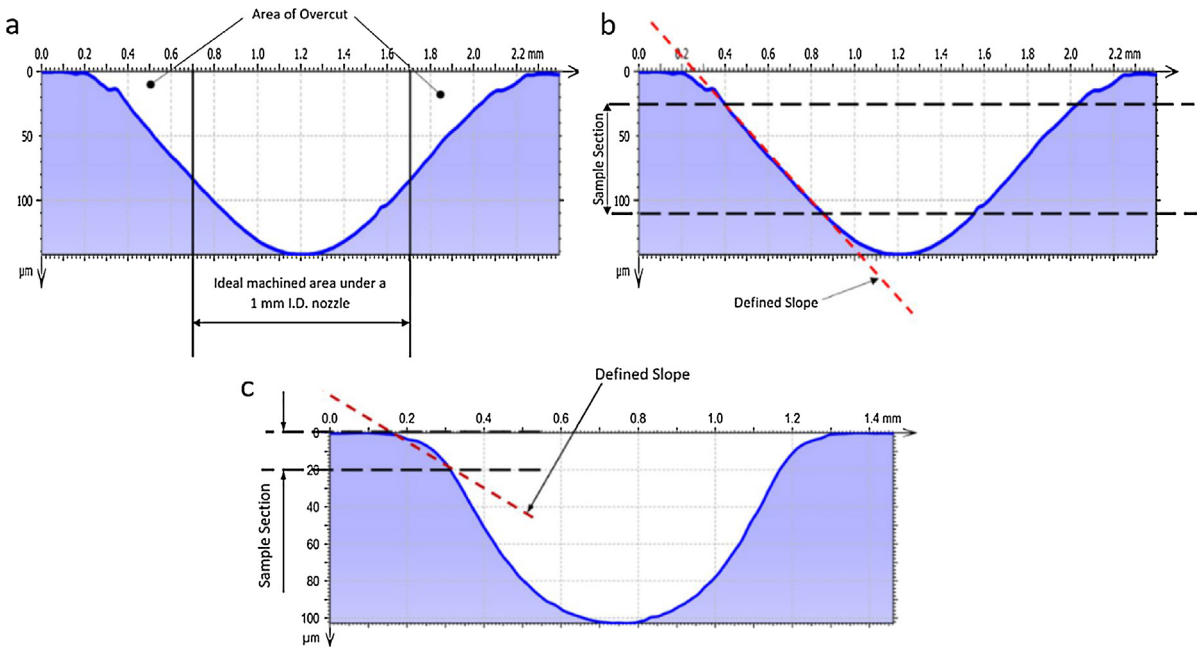

Fig. 2. Schematic to show the definition of the metrics used in this study (a) the definition of overcut (b) definition of sidewall slope and (c) the definition of precision using the top 20% of the total depth.

used, speed was maintained at 0.5 mm/s, except for experiments reported in Fig. 15 where 0.1 mm/s was used.

2.3. Characterisation metrics

In order to assess the response profiles produced several metrics to define the geometrical shape can be applied. The resultant machined profiles of each nozzle type were imaged using a focus variation microscope (Alicona G5 infinite focus, x20 magnification) to create geometrical surface maps. Profiles of the resultant machined features were extracted from these surface maps using DigitalSurf MountainsMap software. Geometrical analysis of the profile data through the software was carried out to obtain depth, defined as the distance from the substrate surface to the maxima of the material removal in the z direction, dissolution kerf, defined as the maximum width of the dissolution region at the substrate surface (Fig. 1c), cross sectional profile area, precision, overcut and side wall slope (taper) of each of the resultant profiles (see Figs. 1c and 2).

Total overcut is defined as the remaining area of the removed profile on both sides of the resultant feature. This is achieved by removing the idealised profile, being the area removed directly below the nozzle, for the full depth of the feature. In the case of Fig. 2a this is 1 mm axially to the nozzle. Minimising overcut is also seen as advantageous within the process as not only does this demonstrate an increase in fidelity of the response profile to that expected, but also makes the process more easily implemented into component design for manufacture.

Slope, (Fig. 2b) is defined in this case as the gradient of the side wall in rise over run format. Side wall slope was extracted from the bulk of the edge ignoring both the radius at the top and bottom of the wall. This is analogous to the taper defined in machining processes and allows comparison between the profiles that are created, greater slope giving a more uniform squarer cross section and a lower slope value giving a more triangulated profile.

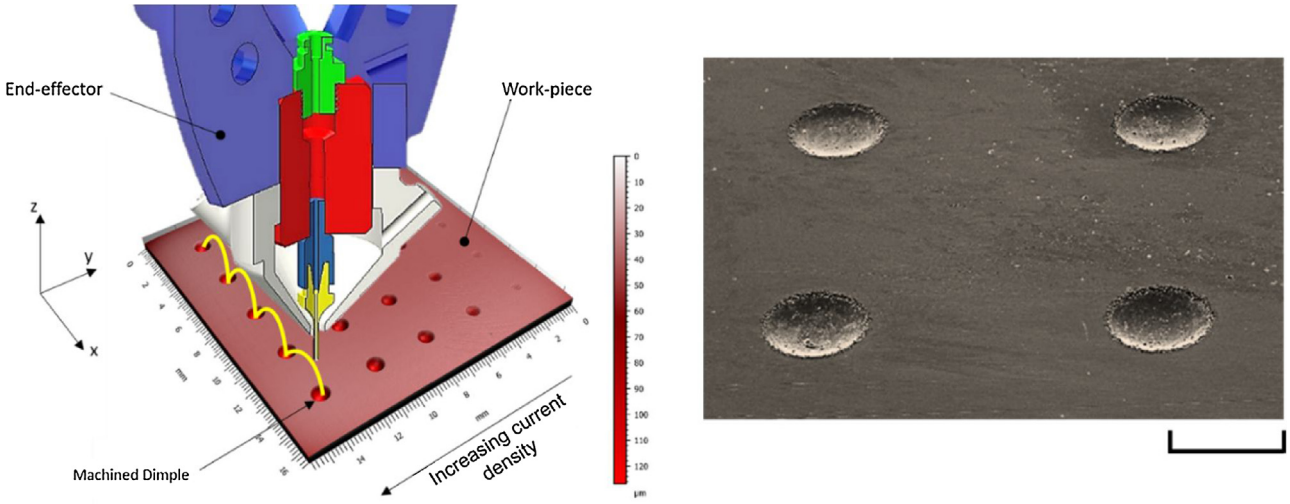

Fig. 3. Schematic of the toolpath used to create dimples and accompanying example SEM image of the resultant features created. Scale bar is 1 mm.

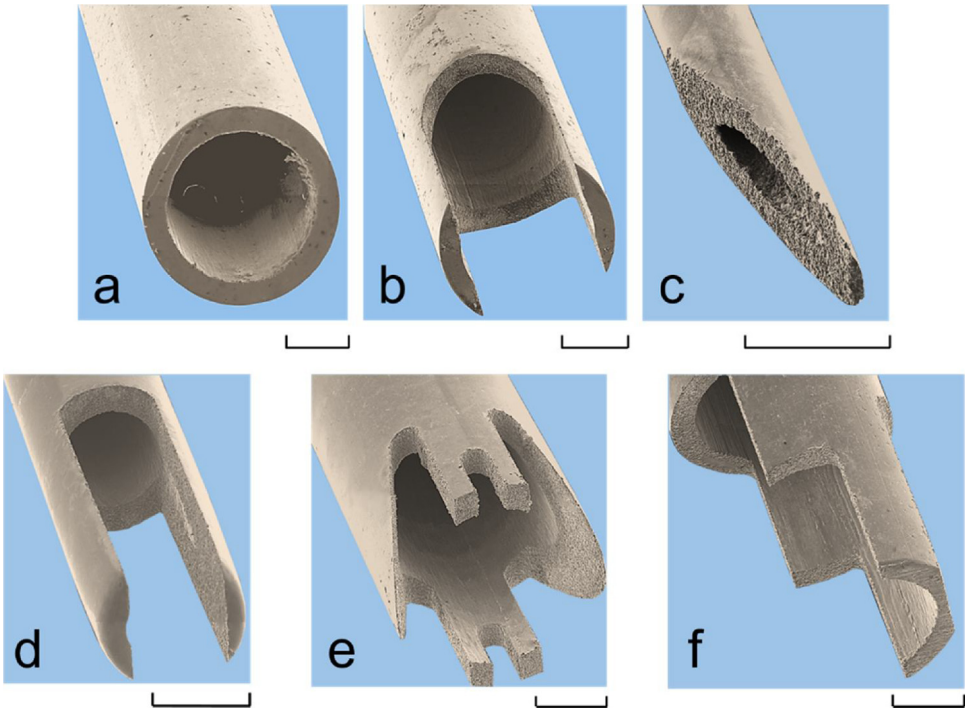

Fig. 4. Nozzle types used within this study (a) standard nozzle (b) 1 mm I.D. symmetrical twin element nozzle (STE), (c) 0.25 mm I.D. off-centre single point nozzle design (OSPE), (d) 0.5 mm I.D. STE nozzle, (e) 1 mm I.D. double channel cut nozzle (DCC) and (f) 1 mm I.D. steps nozzle design. All scale bars 500 um.

In Fig. 2c precision is defined as the slope of the side wall taken to a depth of 20% of the total depth from the top substrate surface. This allows comparison of the individual electrolytes ability to influence low current areas. The greater the slope, the greater the precision, as the un-wanted rounding effects on the shoulder of the cut are minimised and this therefore reflects on the overall kerf dissolution in comparison to the nozzle I.D. Below this threshold, effects from nozzle design and electrolyte ejection have a greater influence.

2.4. Current efficiency testing

To obtain experimentally derived material removal, an array of 5×5 dimples was machined at varying current density levels up to 200 A/cm^2 (Fig. 3). Each dimple was created using a specific toolpath to maintain fidelity to experimental parameters, with a dwell time of 4 s using a standard 0.5 mm I.D. nozzle.

The dimple arrays were then scanned using a focus variation microscope in the same manner as the machined profiles, to obtain the volume of material removed for each current density with different electrolytes; $NaNO_3$, NaCl and the doped electrolyte series. Electrolyte compositions are outlined in Table 2. From the extracted volumes, the experimental material removal can be calculated by incorporation of the material density (Equation 1).

$NaNO_3$ and NaCl were purchased from Scientific Laboratory Supplies Ltd. (UK) and NaI was purchased from Fisher Scientific UK Ltd. All chemicals were analytical grade reagents and were used with no further preparation. Electrolyte solutions were prepared using deionised water. Electrolytes were maintained at 21 °C during all experiments.

2.5. Surface processing

Standardised stainless steel, cylindrical, straight walled nozzles (Fig. 4) with internal diameters (I.D.) of 1 mm, 0.5 mm, 0.25 mm and 0.15 mm were used to demonstrate the electrolyte and as the base for the modified nozzle tip geometries. The nozzle tip modifica-

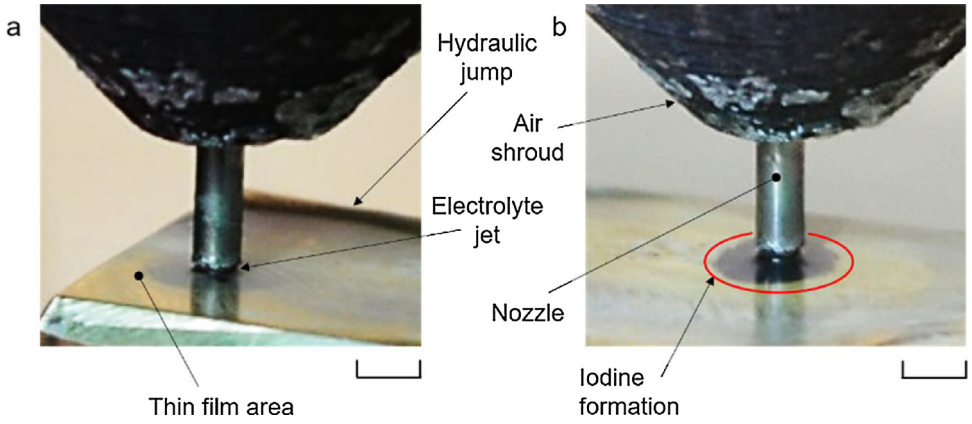

Fig. 5. Photographs of the interaction zones whilst machining at 20 A/cm^2 (a) with $NaNO_3$ (2.3 M) and (b) NaI20 (2.3 M), showing the formation of the iodine radial about the jet zone. Scale bars are 2 mm.

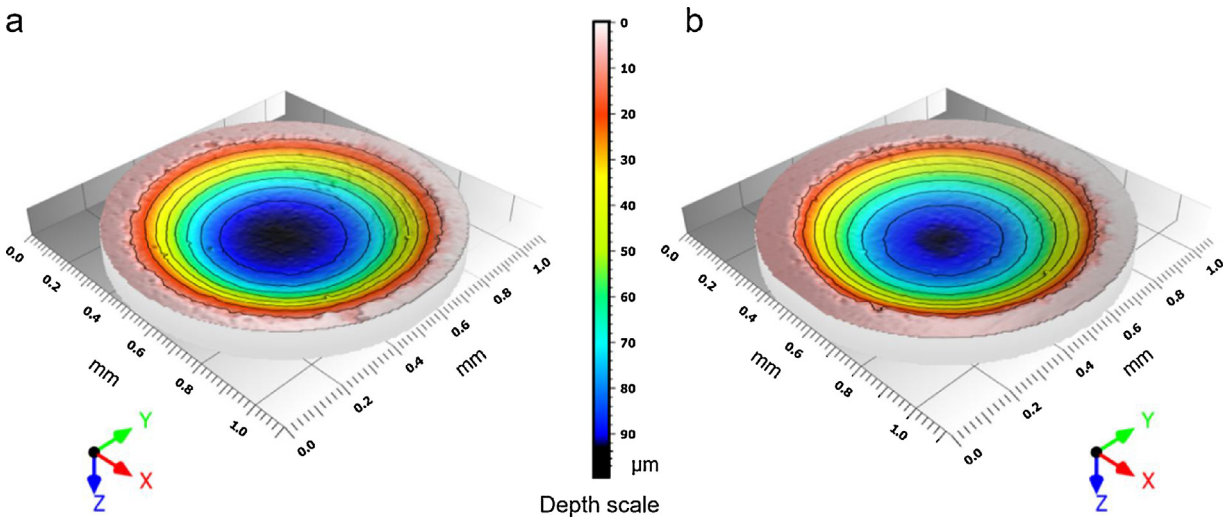

Fig. 6. 3D surface map of compared machined dimples (a) using a 1.8 M solution of $NaNO_3$ and (b) with NaI20.

tions were generated in CAD and toolpaths generated in CAM. Using wire electrical discharge machining (WEDM), the modified geometry was cut into the standard nozzle tips (Fig. 4) using a specially designed jig to ensure symmetry in the geometry.

A previously designed nozzle (Fig. 4b) was employed to highlight areas where the hybrid electrolyte is advantageous in reducing secondary machining zones over a conventional electrolyte. The symmetrical twin element (STE) modified nozzle with an I.D. of 1 mm was employed to create multiple pass striations for comparison of response profiles. Fig. 4d–f shows a range of nozzles used to demonstrate the capability of this methodology to create surface structures with the modified nozzle tips and enhanced electrolyte demonstrating the scalability of the methodology. Fig. 4c being a 0.25 mm I.D. nozzle cut with off-centre single point element (OSPE). Fig. 4d being an STE design except in this instance cut into a 0.5 mm nozzle. Fig. 4e and f are complex nozzle designs cut into 1 mm I.D. nozzles to achieve a specific cut with a secondary smaller indent at the base of the cut and minimised taper.

3. Surface processing

3.1. Enhanced precision

In Fig. 5 an effect of NaI addition to the electrolyte can be observed. In Fig. 5b iodine can be seen to be forming under the jet impingement area as a dark cloud, in comparison to Fig. 5a, where only $NaNO_3$ was used. Here no coloration of the thin film area is observed. It is interesting to note that iodine saturation within the electrolyte thin film, is visible up to 2 mm from the nozzle axis, where the iodide is oxidised. This is well within the resistive thin film area, where the current developed is extremely low and material removal would not occur.

The justification for the selection of NaI as a dopant can be seen in Fig. 6 where exemplar 3D surface maps generated from an areal scan of dimples are presented. Fig. 6a demonstrates a dimple created with a 1.8 M solution of $NaNO_3$ showing the contour lines corresponding to the colour-scale changes. In Fig. 6b identical pro-

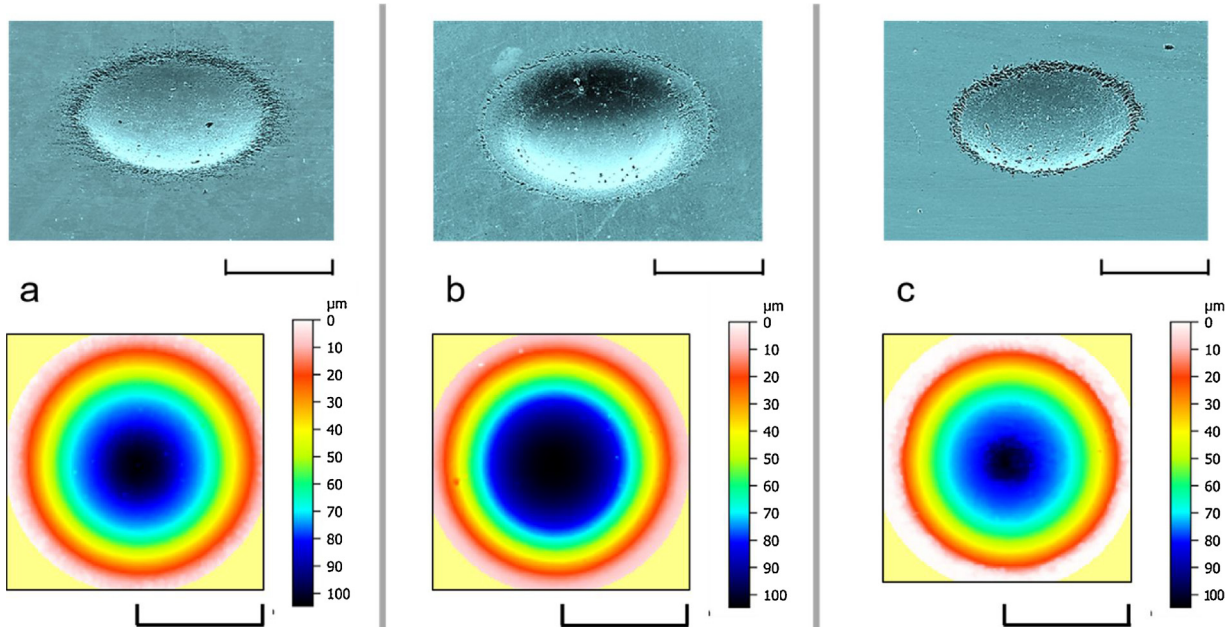

Fig. 7. Tinted SEM images tilted at 60° of machined pits and associated contour information from surface scans of dimples machined at 200 A/cm^2 in (a) $NaNO_3$ (b) NaCl (c) NaI10. Scale bars 500 µm.

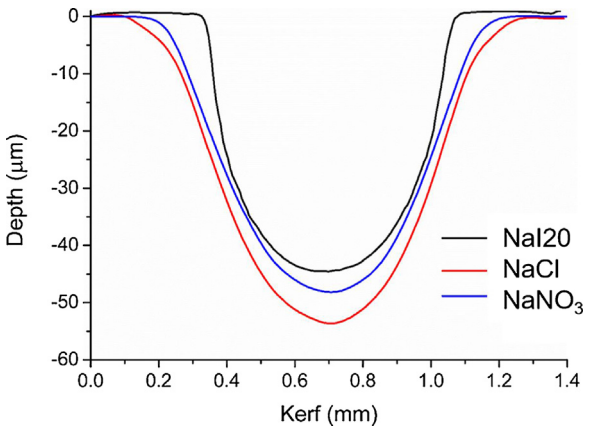

Fig. 8. Comparison of machined profiles using 3 different electrolytes. Profile scans taken from the dimples produced using a standard nozzle at 100 A/cm^2.

cess parameters were used but NaI was added to the electrolyte solution, to make a 2.3 M solution (NaI20, Table 2).

Prior research [31] has identified that a reduction in electrolyte concentration leads to an increase in precision. However, in this case, although the concentration and conductivity has increased in Fig. 6b with the addition of NaI, a 10% reduction in area of the dimple profile from 62541 μm^2 (SD < 1%) to 56128 μm^2 (SD < 1%) has occurred, recalling Table 2. This change in area can be seen in Fig. 6, the reduction in rounding at the surface to feature interface on 6b compared to 6a and the wider flatter bottom to the base resulting in a steeper side wall to the dimple.

In Fig. 7 SEM of dimples machined with 200 A/cm^2 using three different electrolytes $NaNO_3$ (a), NaCl (b) and NaI10 (c) are shown. These are accompanied with respective surface scans. The obvious difference is observed in the SEM images at the shoulder interface of the dimple to substrate surface. Comparing the red contour band of all three images the enhanced electrolyte shows a thinner more defined band at which the same gradient occurs at a shallower depth range.

When the precision metric (as defined in section 2.3) of three samples are compared, the enhanced electrolyte shows a mean slope of 0.373 μm/μm (SD 5.3%) achieving a 149% increase when compared to the NaCl electrolyte (0.15 μm/μm SD 4.8%) and 96% when compared to the $NaNO_3$ electrolyte (0.19 μm/μm SD 7.8%). It is worth noting that chloride, although exhibiting the worst geometry definition of the three electrolytes, achieves a greater machining depth of 104 μm (SD <1%) compared to 92 μm (SD 1.7%) for the $NaNO_3$ and 90 μm (SD 2%) for the NaI10. This is a result of the consistently high current efficiency of this electrolyte across a broad range of current densities.

The resultant profiles seen in Fig. 8, machined with the standard nozzle at 100 A/cm^2, continues to demonstrate the same trend in the enhancement of the geometry definition at the dimple shoulder despite the reduction in applied energy. A reduction in overcut of 59% is seen when NaI20 is used (2607 μm^2 SD 5.8%) as compared to NaCl (6377 μm^2 SD <1%). A 43% reduction is also observed when compared to $NaNO_3$ (4544 μm^2 SD 6%).

This change in the removal profile in comparison to $NaNO_3$ occurs at all current densities tested in this study. This is consistent with the hypothesis for this work that some energy will be preferentially utilised in oxidation of the dopant as opposed to direct machining. It should be noted that for this reason, iodide enhanced electrolytes are not recommended in applications whereby high material removal rates are sought over process dimensional accuracy. This is demonstrated in Fig. 9 where the precision metric defined in section 2.3, which reflects on the overall dissolution kerf, obtained from dimples at 200 A/cm^2 is compared to the material removal rate (MRR) across the range of electrolytes tested.

The trend can be seen whereby NaCl demonstrates the highest removal rate at 0.078 mg/s (SD <1%) then decreasing by 8% to 0.069 mg/s (SD 2.4%) with the use of $NaNO_3$. MRR is reduced by the introduction, and increasing NaI concentration, culminating in a reduction of 34% in the MRR compared to the straight $NaNO_3$ solution with NaI40 having an MRR of 0.046 mg/s (SD <1%). Therefore, for every 1% increase in NaI added there is approximately a 1.2% decrease in MRR. Conversely, precision is seen to increase from NaCl showing the lowest slope at 152 μm/mm (SD 4%) to a 25% increase with the use of $NaNO_3$ (190.8 μm/mm SD 7%). Culminating with a 206% increase in precision when a 20% addition of NaI is used (583.6 μm/mm SD 7%) compared to a straight $NaNO_3$ solution and 284% increase when compared to NaCl. Precision can be seen to

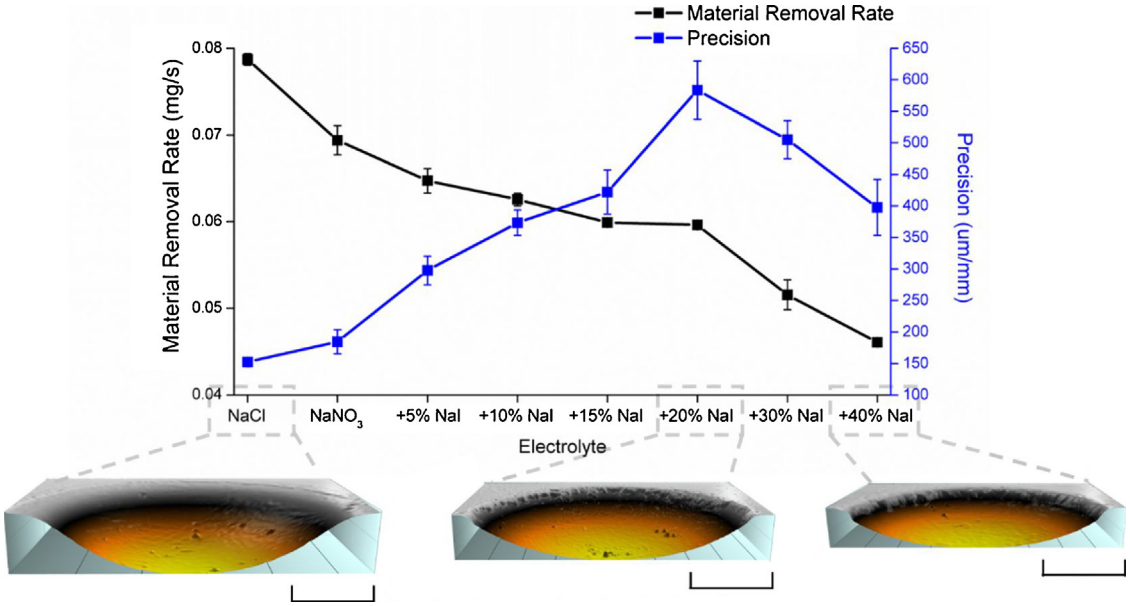

Fig. 9. Comparison of material removal and precision across the variation of electrolytes at 200 A/cm^2 Reconstructed and sectioned 3D images of exemplar machined dimples from the samples machined with NaCl, NaI20 and NaI40 all represented on the same scale. All scale bars are 250 μm.

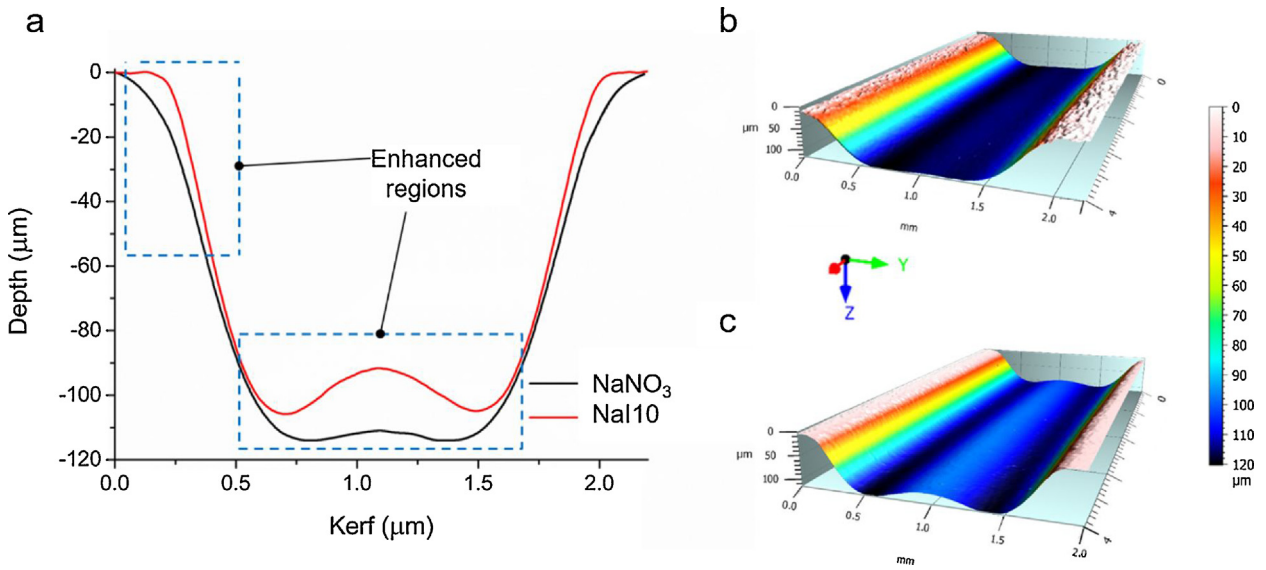

Fig. 10. (a) Comparison of $NaNO_3$ and NaI10 profiles produced with an STE nozzle used over 4 passes demonstrating the increase feature fidelity in discrete areas that can be achieved when used with a modified nozzle and hybrid electrolyte. (b) 3D reconstruction of a sample cut with an STE nozzle and $NaINO_3$ (c) 3D reconstruction of a sample cut with an STE nozzle and NaI10.

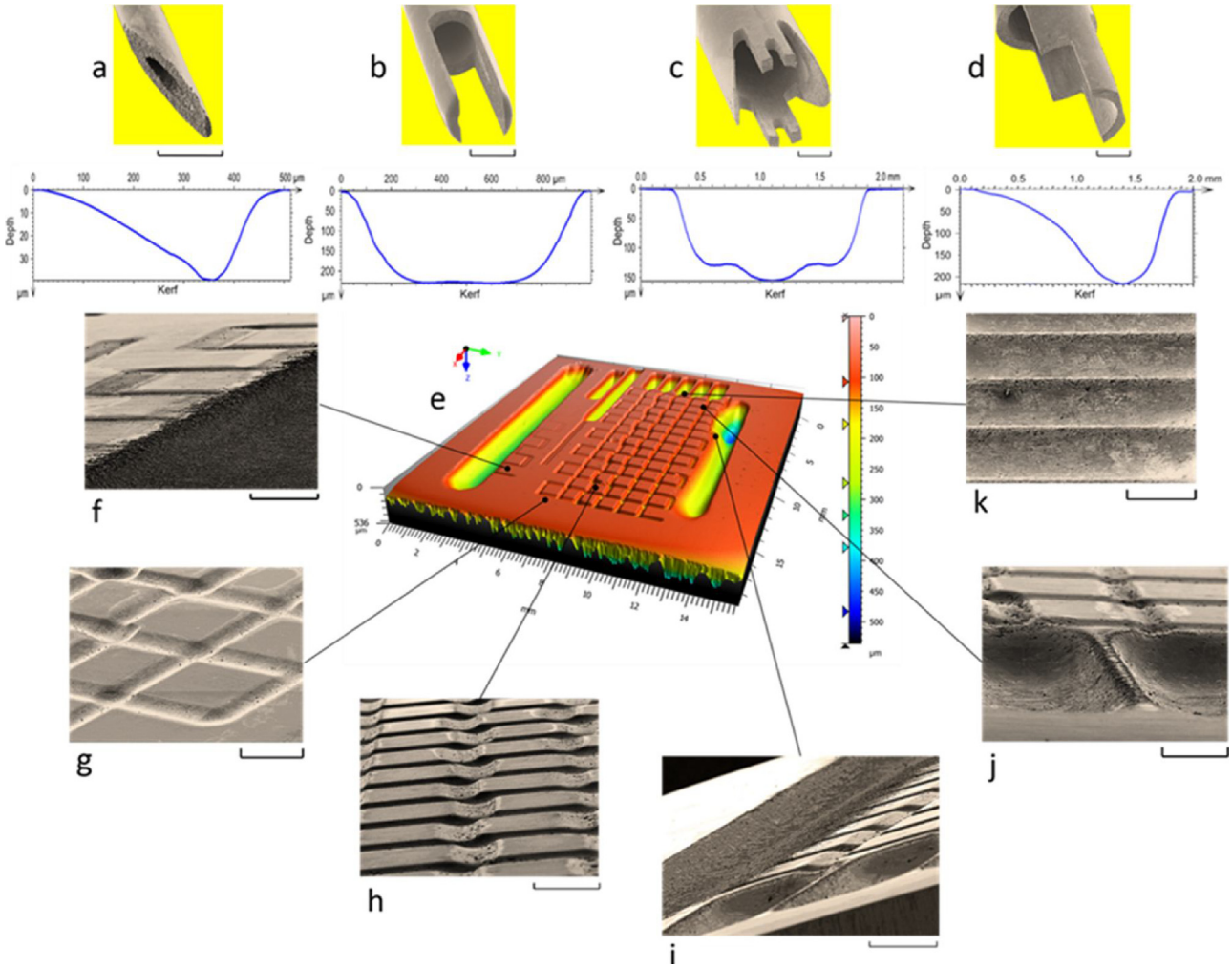

Fig. 11. All features were machined using NaI10 and applied to varying nozzle designs at differing scales (a) 250 μm I.D. nozzle cut with an OSPE geometry and the resultant profile shown below. (b) 500 μm I.D. nozzle with resultant geometry below. (c, d) 1 mm nozzle cut with an intentionally complex pattern to test the fidelity of the profile that can be created with the resultant profile below. (e) Shows a scanned surface map converted into a 3D image where all the above nozzles have been used to create features. (f) From the trench created by nozzle c. (g) and (h) using nozzle (a) in two differing directions giving a different effect in both directions. (i) Deep pits created by nozzle (b) next to patterning created by nozzle (a) going into deep trench created by nozzle (d). (j) Nozzle (a) leading from pits created by nozzle (b). (k) Ribs created by nozzle (b). All scale bars are 500 μm.

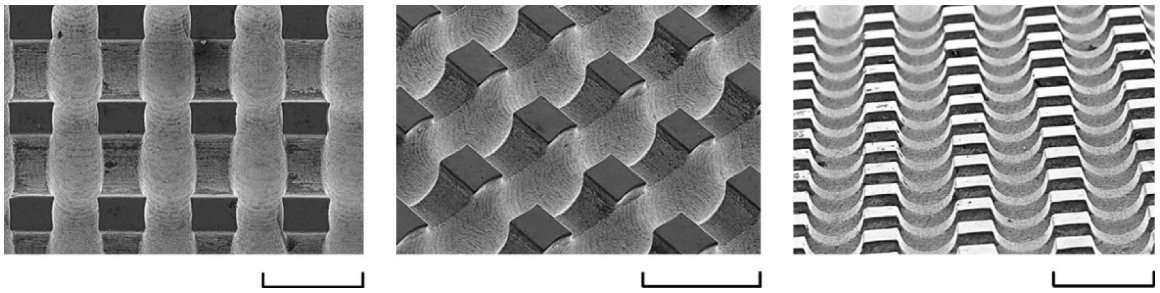

Fig. 12. SEM images of repeating surface structures developed to demonstrate process capability for enhanced adhesion. Machining undertaken with a 0.15 mm I.D. nozzle. All scale bars are 500 μm.

improve by 50% for every 5% extra ratio of NaI that is added up to this point, beyond which precision appears to decrease at this current density level. As material removal becomes reduced at this current density level, the dimple profile area drops to 47200 μm^2 (SD <1%) for NaI40 compared to 55700 μm^2 (SD <1%) for NaI20, meaning the side wall slope is very low and is reflected in the evaluated precision. Therefore beyond 20% inclusion of NaI, the reduced MRR is not off-set by increased precision making this the most favoured option at this current density.

3.2. Enhanced feature generation

The application of more complex nozzle designs to affect a distinct profile demonstrates the enhancements that are achievable through implementation of the doped electrolyte. When the electrolytes are couple with modified nozzle tips the increase in fidelity of the response profile to the nozzle tip geometry is exaggerated. In the case of Fig. 10a, an STE nozzle is used over 4 passes. Several distinct areas of change are observed. Firstly, a reduction in width by 10% to 1.74 mm (SD <1%) with the NaI10 electrolyte. Secondly, the slope on the side walls can also be seen to increase by 34% to 0.35 μm/μm (SD 2.4%). Furthermore, the radius at the shoulder and apex of the troughs is reduced giving a reduction in overcut of 14% from 40181 μm^2 (SD 2.2%) to 34496 μm^2 (SD 1.8%).

Profiles in Fig. 10 show that even when used with an enhanced electrolyte there is a limit to the precision of the geometry that can be achieved. It is apparent though, that these features influence the overall profile created since they are significantly different to those generated with the equivalent $NaNO_3$ electrolyte. The fidelity to the intent from the nozzle design is also influenced by secondary factors which includes hydrodynamic and changing resistance profiles as the cut feature evolves. This is in contrast to other energy beam techniques where the end-effector geometry directly denotes the response profile.

In Fig. 11, the innovation demonstrated previously is deployed for the purpose of demonstrating the new capabilities available to EJP practitioners. Here, Inconel 718 is processed using a number of nozzles with NaI10 electrolyte to investigate the application of previously generated geometries on a smaller scale and to investigate the fidelity of features that can be achieved using complex nozzle designs.

The principle of nozzle design is applied to create an *OSPE* type geometry on a 250 μm nozzle (Fig. 11a) and *STE* geometry on a 500 μm nozzle (Fig. 11b). In doing so the scalability of this technique is highlighted. Using smaller nozzles leads to reduced kerf width while maintaining the desired profile. Utilising higher jet speeds, current densities (~400 A/cm^2) and slower head traverse speeds (~0.1 mm/s) to obtain enhanced precision features with these smaller nozzles, Fig. 11e.

New nozzle designs were also realised to test the ability of the process to maintain profile fidelity. Figures 11e-k show a surface scan transposed into a 3D image and accompanying SEM images. This demonstrates how response profiles can be combined, through superimposition, to create an application-ready surface, for example, in microfluidic reactors, biomimetic surfaces or mechanical interlocking interfaces. Complete surface processing was undertaken in under 45 min including nozzle changes. The use of additional tooling was not required. All four profiles seen in Fig. 11a–d were taken from this sample and demonstrate both the depth and profile achieved by a single pass.

Fig. 12 shows the application of the enhanced electrolyte with a standard 150 μm nozzle to create repeated surface structures with sharp angular interfaces required for an enhanced adhesion surface application. Although the rounded base is still prevalent due to the use of a standard nozzle, sharpness of the feature-to-surface-interface and reduced taper at the top section of the profile is obvious. The slight undercut and curved top edge created in one direction occurs because of hydrodynamic effects. Upon successive machining passes the recessed regions are exposed diverting ejecting fluid flow. This effect can be minimised or exploited by careful consideration of the toolpath and associated process parameters.

4. Process mechanics

From the results obtained through experimentation the enhancement to precision and fidelity of the resultant features created is obvious through the range of NaI-doped electrolytes used. The removal effects in the first instance appear to concur with the original hypothesis. However, the increasing conductivity of the NaI–doped electrolytes (Table 2) as the concentration increases the resultant profiles demonstrate a counterintuitive trend of significantly reducing MRR. The mechanism involved therefore requiring greater investigation.

4.1. Current filtering

Improvements can start to be explained by consideration of current efficiency characteristic of each electrolyte (Fig. 13a). Here individual electrolyte current efficiency has been obtained from experimental comparison to theoretical values as outlined in Section 1.2 and using Equation 1. There is a stark difference in current efficiency at the lower current densities (< 60 A/cm^2) between the electrolytes. In comparison to NaCl, all the $NaNO_3$ based electrolytes exhibit a much lower efficiency at low current densities. It is worth noting that it was deemed at this point not to take the inclusion of NaI further than 40% due to low MRR at these current density levels and the cost implications for large-area processing. At 20 A/cm^2, NaI20 exhibits an efficiency of 1.3% (SD < 1%) in comparison to NaNO3 at 26% (SD < 1%) efficiency, and NaCl at 66% (SD 1.3%) efficiency. In comparison, at 200 A/cm^2, NaI20 exhibits an efficiency of 62% (SD < 1%), when compared to $NaNO_3$ at 73% (SD 1.8%), and NaCl at 84% (SD < 1%).

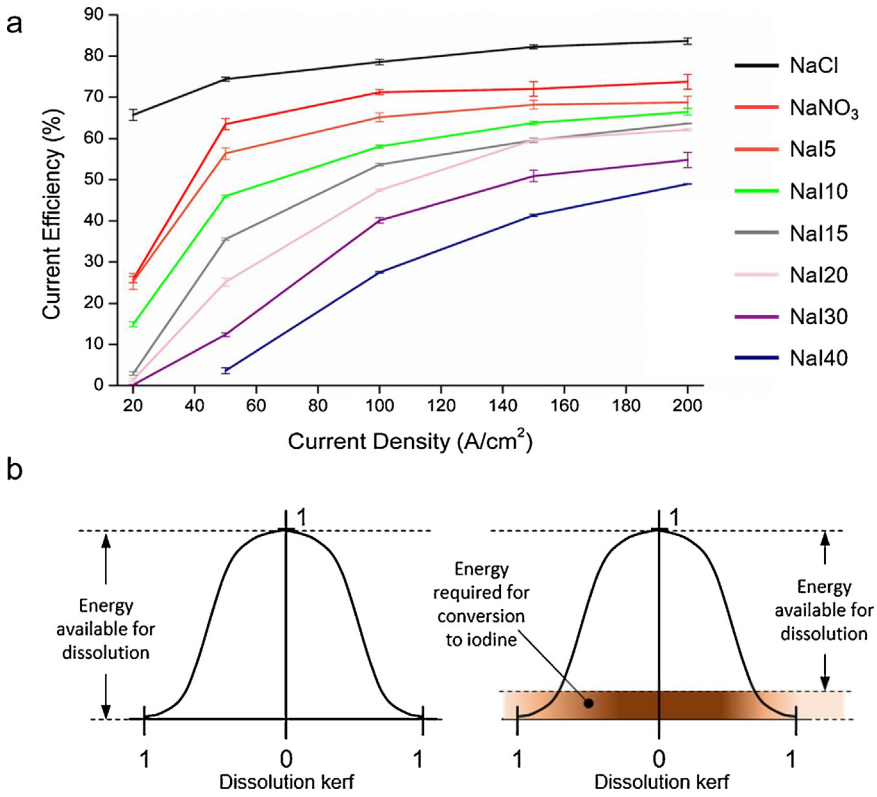

Fig. 13. Energy filtering mechanism description (a) comparison of electrolyte efficiency across the range of electrolytes tested including increasing ratios of NaI (b) description of the mechanism occurring leading to exclusion of current levels at discrete points in the energy distribution, the machined profile being the mirror of the energy density curve.

Since the current efficiency at low mean current density is lower for the NaI-doped electrolytes, the threshold energy required for material removal is not achieved at the periphery of the feature. Hence, material removal is inhibited in these secondary machining zones, and a sharper edge definition is observed, shown by the highlighted regions in Fig. 10a. This can then be compared to the higher current density areas at the centre of the pit where the efficiency differential between electrolytes is markedly reduced. Therefore, the energy density profile will demonstrate a steeper slope for the enhanced electrolyte resulting in less overcut as shown by the mechanism schematic in Fig. 13b whereby the resultant machined profile will be a mirror of the energy density curve.

This phenomenon can be further observed in Fig. 14, where 3 lines were machined with mean current densities increasing from 4 A/cm^2 to 50 A/cm^2 in 3 mm steps at 0.5 mm/s. The lines were machined with $NaNO_3$, NaI20 and NaI40.

It can be observed from Fig. 14 that as the current density increases from left to right, the filtering effect of the NaI addition can be clearly seen. The $NaNO_3$ (control) line showing an initial light texturing effect at 4 A/cm^2 as the dissolution energy required for the material is reached. From that point on the texturing continues to become more defined to 32 A/cm^2 where the mechanism has stabilised and becomes a consistent width. In comparison, the lines for NaI20 and NaI40 demonstrate very different regimes. The Gaussian energy distribution is acutely obvious as surface texturing starts to appear at the point where the energy distribution is highest in the centre of the jet and filling out to the width of the final line as current increases, noting the reduced width of the textured area in comparison to the $NaNO_3$ throughout. The NaI20 line

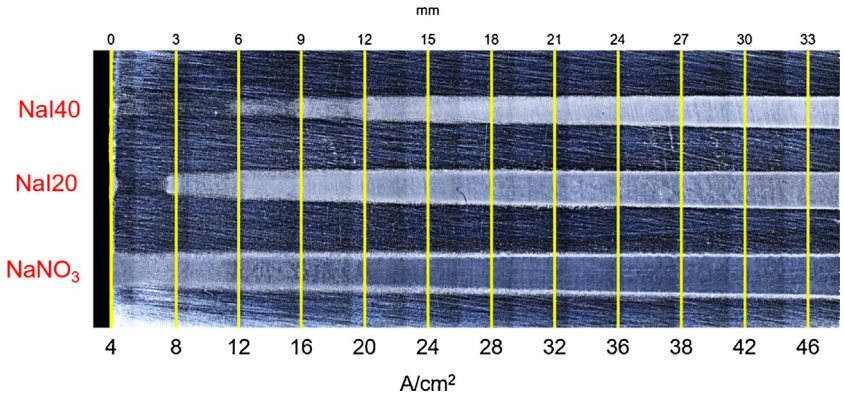

Fig. 14. Optical micrograph of three machined lines all using the identical toolpaths and machine parameters but with differing electrolytes, to demonstrate the point at which the applied current exceeds the energy filter required to initiate dissolution of the material.

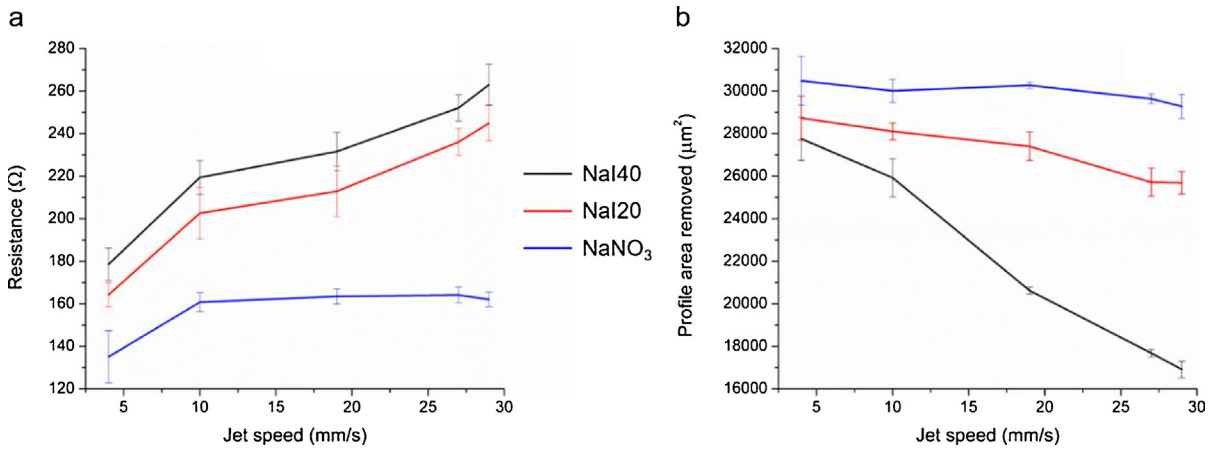

Fig. 15. impact of variation of electrolyte jet speed on (a) in-process resistance and (b) profile area removed with differing electrolytes.

surface initiating dissolution at 8 A/cm^2 and achieving a consistent line width by 36 A/cm^2. The NaI40 line starts to achieve dissolution a step further on than the NaI20 line at 12 A/cm^2, although with a much lighter and thinner texturing. In line with this, the NaI40 electrolyte does not achieve a consistent line until 1 step beyond the NaI20 at 38 A/cm^2. The difference in dissolution kerf, pertaining to precision can again by observed with the $NaNO_3$ line having a final width of 1.97 mm in comparison to the NaI20 of 1.69 mm and the NaI40 of 1.45 mm demonstrating a 26% reduction for the NaI40 electrolyte.

The increased suppression of current efficiency at low current densities through increasing concentration of NaI (0–40%) is understood to be a result of beneficial Faradaic losses within the anodic oxidation process. The reduction in current efficiency is not dependent on electrolyte conductivities. This assertion is supported by the measured conductivities (Table 2), and the known linear relationship between electrical potential as defined by Ohms law. In addition, equimolar ionic strength solutions were used throughout this study, with all electrolytes having similar theoretical activity coefficients.

Iodide is a strong reducing agent (E^o $2I^- \rightarrow I_2 = -0.62$ V vs. SHE). This is especially pertinent in comparison to commonly used chloride ($E^\circ Cl^- \rightarrow Cl_2 = -1.40$ V vs. SHE) containing electrolytes, such as NaCl [48]. It is proposed that this readiness of iodide anions to undergo oxidation to molecular iodine presents a relatively facile route through which energy that would otherwise be devoted to the electrolytic oxidation of nickel (material removal) (E^o $Ni \rightarrow Ni^{2+} = 0.26$ V vs. SHE) and other alloying elements, is transferred. This competing electrode reaction supresses the anodic dissolution of the nickel-based substrate, leading to the experimental observation of a machining cut-off point; manifested in a current density below which the current efficiency approaches 0%. This cut-off point is different for each electrolyte tested and increases with iodide concentration. The addition of iodide at varying concentrations therefore leads to greater aspect ratio features, superior edge definition, and reduced overcut. It should be noted that this is effect is also dependent upon the work piece material.

4.2. Refresh rate

In order to further assess the mechanism leading to increased precision, a series of experiments were conducted varying the electrolyte jet speed across the range available; 4, 10, 19, 27 and 29 m/s. Considering Fig. 15, where resistance and removed profile area are compared to jet speed, a second influencing mechanism can be identified in relation to the Faradaic filtering effect, relating to the iodide concentration at the work surface. It is shown in Fig. 15a that as the electrolyte jet speed is increased there is negligible change in the in-process resistance experienced in the IEG, for $NaNO_3$ electrolytes, beyond the initial increase up to 10 m/s associated with a transition in debris clearance regimes [13]. In comparison, the NaI-doped electrolytes have higher, and increasing, resistance with jet speed. This is counterintuitive since the conductivity of these electrolytes exhibits the opposite resistance trend. This is attributed to the readiness with which the transitory iodine mask forms in these electrolytes. At the highest jet speed, with a constant J of 100 A/cm^2, the NAI40 electrolyte shows a 62% increase from 162 Ω (SD 2.2%) to 263 Ω (SD 3.6%).

In conjunction with this, in Fig. 15b the relationship with jet speed to the area removed can be observed. The $NaNO_3$ electrolyte displays a negligible change in area removal of 4% (SD 2%) over the range of jet speeds, the NaI20 in comparison demonstrates a 9% (SD 2%) reduction in area from the lowest to highest jet speeds. However, the NaI40 experiences a drop of 39% (SD 2%) over the jet speed range having an area 42% (SD 2.2%) less than $NaNO_3$ at 29 m/s.

From these results, the second influencing mechanism can be elucidated; the refresh rate. It is clear that the concentration of iodide present in the feedstock is not the only contributing factor, but also the rate at which it is refreshed at the surface. The higher the iodide refresh rate (consistent with increased jet speed), the greater the proportion of energy diverted from material removal to iodide oxidation.

4.3. Incident iodide concentration (IIC)

In order to appraise these two influences, a simple metric can be developed, the incident iodide concentration (IIC) (Eq. (2)) expressed in mol/s.

$$IIC = \dot{V}_{jet} \cdot M \tag{2}$$

Where $\dot{V}_{jet}$ is the volumetric flow rate (ml/s) of the electrolyte jet and M is the concentration of any given doping agent in each electrolyte case. Fig. 16 shows the IIC as a function of NaI concentration, in this case, and increasing pump speed. This allows comparison between different iodide concentrations and pump speeds and relates directly to the area removed and precision of the feature created.

The extracted areas (Fig. 16b and c) show exemplar profiles and the associated geometrical information taken across the same IIC number. Although it would be expected that the profiles would be similar, these demonstrate there is some variance in the actual in comparison to calculation. The total area is comparable with only a 4% difference however there are differences in the precision

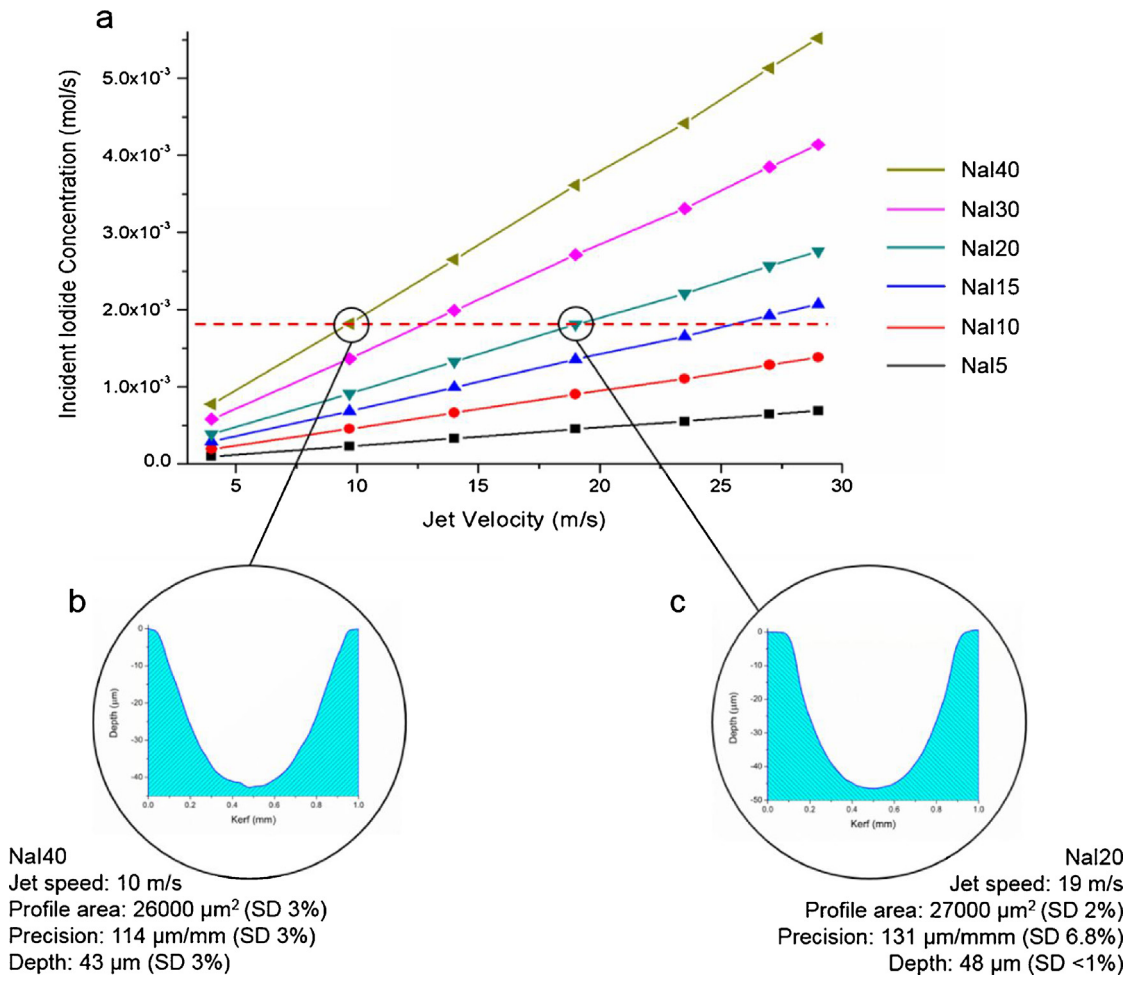

Fig. 16. Comparison of ICC to actual feature geometry (a) Graph generated from Equation 2 depicting ICC as a function of jet speed and NaI concentration (b) exemplar profile machined at 100 A/cm^2 using NaI40 with 10 m/s jet speed and mean geometry information from samples (c) exemplar profile machined at 100 A/cm^2 using NaI20 with 19 m/s jet speed and mean geometry information from samples.

and depth. This can be explained when comparing the geometry changes as jet velocity increases of the same experiments using a $NaNO_3$ electrolyte. The $NaNO_3$ electrolyte experiences a 31% increase in precision with increasing jet speed from 10 m/s to 19 m/s in comparison to a 15% increase in precision between NaI40 and NaI20 at the same IIC. The depth having a mean increase of 11% for the NaI based electrolytes compared to 6% increase for the $NaNO_3$. This is likely due to hydrodynamic effects of increased jet speed aiding debris removal and helping to concentrate the jet impingement area which can be seen in the shape of the response profiles. The NaI-doped electrolytes displaying a lesser increase in precision, due to limits to the precision that can be achieved, observing that the lower speed NaI40 still maintains a mean increase of 7% precision over the higher jet speed $NaNO_3$.

5. Conclusions

It has been demonstrated through this work, that the use of an iodide-doped electrolyte within electrochemical jet processing techniques achieves a transitory filtering effect. This leads to a limitation of low-level current associated with poor precision.

Dimensional accuracy improvements, such as lower side wall taper, and superior surface intersection result from the use of these iodide-enhanced electrolytes, leading to modulated activation thresholds. It is observed that approximately, for every 1% increase in NaI there is a 1.2% decrease in MRR and conversely there is a 206% increase in precision when a 20% addition of NaI is used compared to a $NaNO_3$ solution, and 284% increase when compared to NaCl electrolytes at the equivalent ionic strength. Furthermore, the discrete response profiles when used with complex nozzles are exaggerated due to the enhanced energy density differential perceived at the work surface.

Through this work, the concept of current filtering and re-fresh rate is introduced to explain the process mechanics involved leading to increases in precision and fidelity through the inclusion of sodium iodide in a doped electrolyte.

The metric of the incident iodine concentration (IIC) is introduced to demonstrate how the process mechanics can be combined and evaluated.

This study has demonstrated that a step change in process fidelity and flexibility can be achieved through optimisation of the electrochemistry specific to jet processes.

Acknowledgements

This work was supported by the Engineering and Physical Sciences Research Council [grant numbers EP/M02072X/1, EP/L016206/1] through the “In-Jet Interferometry for Ultra Precise Electrolyte Jet Machining” project, and the EPSRC Centre for Doctoral Training in Innovative Metal Processing. The authors would like to thank the Manufacturing Metrology Team, and the Nanoscale and Microscale Research Centre at the University of

Nottingham for providing access to the metrology equipment for surface measurement, and for access to electron microscopy, and Matthias Hirsch and Alexander Jackson-Crisp of ACEL for technical assistance with surface scanning.

References

[1] Shu LH, Ueda K, Chiu I, Cheong H. Biologically inspired design. CIRP Ann Manuf Technol 2011;60:673–93.
[2] Han Z, Mu Z, Yin W, Li W, Niu S, Zhang J, et al. Biomimetic multifunctional surfaces inspired from animals. Adv Colloid Interface Sci 2016;234:27–50.
[3] Malshe A, Rajurkar K, Samant A, Hansen HN, Bapat S, Jiang W. Bio-inspired functional surfaces for advanced applications. CIRP Ann Manuf Technol 2013;62:607–28.
[4] Bruzzone AAG, Costa HL, Lonardo PM, Lucca DA. Advances in engineered surfaces for functional performance. CIRP Ann Manuf Technol 2008;57:750–69.
[5] Chen Q, Pugno NM. Bio-mimetic mechanisms of natural hierarchical materials: a review. J Mech Behav Biomed Mater 2013;19:3–33.
[6] Egan P, Sinko R, LeDuc PR, Keten S. The role of mechanics in biological and bio-inspired systems. Nat Commun 2015;6:7418.
[7] Hansen HN, Hocken RJ, Tosello G. Replication of micro and nano surface geometries. CIRP Ann Manuf Technol 2011;60:695–714.
[8] Zhang F, Chan J, Low HY. Biomimetic, hierarchical structures on polymer surfaces by sequential imprinting. Appl Surf Sci 2008;254:2975–9.
[9] Gandhi R, Moreno C, Wang Z, Chang C, Saldana C, Mann JB. Novel methods for scalable manufacturing of micro-textured surfaces. IIE Ann Conf Expo 2014;(2014):3757–64.
[10] Kunieda M. Influence of micro indents formed by electro-chemical jet machining on rolling bearing fatigue life. ASM, PED 1993;1993(64):693–9.
[11] Bocking CB, Sl Dover, Bennett G. An investigation into the suitability ofhigh speed selective jet electrodeposition for rapid tooling. First National Conference on Rapid Prototyping and Tooling Research: MEP 1995:157–73.
[12] Kunieda M, Katoh R, Mori Y. Rapid prototyping by selective electrodeposition using electrolyte jet. CIRP Ann Manuf Technol 1998;47:161–4.
[13] Mitchell-Smith J, Speidel A, Gaskell J, Clare AT. Energy distribution modulation by mechanical design for electrochemical jet processing techniques. Int J Mach Tools Manuf 2017;122:32–46.
[14] Hackert M., Meichsner G., Schubert A., 2008. Generating Micro Geometries with Air assisted Electrochemical Machining. In: H. van Brussel EB, H. Spaan, T. Burke, editor. EUSPEN 10th International Conference. Zurich, p. 5.
[15] Hackert-Oschätzchen M, Meichsner G, Zeidler H, Zinecker M, Schubert A. Micro machining of different steels with closed electrolytic free jet. In: AIP Conference Proceedings. 2011. p. 1337–43.
[16] Kunieda Mea Study of Electrolyte Jet Machining of Cemented Carbide. In: Hinduja SL, L., editor. Proceedings of the 37th International MATADOR Conference: Springer London, 2012.
[17] Hackert-Oschätzchen M, Martin A, Meichsner G, Zinecker M, Schubert A. Microstructuring of carbide metals applying jet electrochemical machining. Precision Eng 2013;37:621–34.
[18] Mitchell-Smith J, Murray JW, Clare AT, Kunieda M. In: Bahre D, Rebschlager A, editors. Electrolyte jet machining for surface texturing of inconel 718. Saarbrucken, Germany: INSECT 2014; 2014. p. 111–8.
[19] Mitchell-Smith J, Clare AT. ElectroChemical jet machining of titanium: overcoming passivation layers with ultrasonic assistance. Procedia CIRP 2016;42:379–83.
[20] Liu W, Ao S, Li Y, Liu Z, Zhang H, Manladan SM, et al. Effect of anodic behavior on electrochemical machining of TB6 titanium alloy. Electrochim Acta 2017;233:190–200.
[21] Speidel A, Lutey AHA, Mitchell-Smith J, Rance GA, Liverani E, Ascari A, et al. Surface modification of mild steel using a combination of laser and electrochemical processes. Surf Coat Technol 2016;307(Part A):849–60.
[22] Kunieda M, Ooshiro S, Iwamoto N. Manufacturing dimpled saw wires using electrolyte jet machining. J Jpn Soc Precision Eng 2010;76:572–6.
[23] Kunieda M. Injection molding transcription of micro surface structure machined by EJM. Japan society for precision engineering. Academic lecture Conference Paper Collection 2013:867–8.
[24] Schubert A, Neugebauer R, Sylla D, Avila M, Hackert M. Manufacturing of surface microstructures for improved tribological efficiency of powertrain components and forming tools. CIRP J Manuf Sci Technol 2011;4:200–7.
[25] Schubert A, Hackert-Oschätzchen M, Meichsner G, Zinecker M. Design and realization of micro structured surfaces for thermodynamic applications. Microsyst Technol 2011;17:1471–9.
[26] Walker JC, Kamps TJ, Lam JW, Mitchell-Smith J, Clare AT. Tribological behaviour of an electrochemical jet machined textured Al-Si automotive cylinder liner material. Wear 2017;376–377(Part B):1611–21.
[27] Speidel A, Mitchell-Smith J, Walsh DA, Hirsch M, Clare A. Electrolyte jet machining of titanium alloys using novel electrolyte solutions. Procedia CIRP 2016;42:367–72.
[28] McGeough JA. Advanced methods of machining. UK: Chapman and Hall Ltd.; 1988.
[29] Datta M, Landolt D. On the influence of electrolyte concentration, pH and temperature on surface brightening of nickel under ECM conditions. J Appl Electrochem 1977;7:247–52.
[30] Bhattacharyya B. Chapter 2 – electrochemical machining: macro to micro. In: Electrochemical micromachining for nanofabrication, MEMS and nanotechnology. 2015: William Andrew Publishing; 2017. p. 25–52.
[31] De Silva AKM, Altena HSJ, McGeough JA. Influence of electrolyte concentration on copying accuracy of precision-ECM. CIRP Ann Manuf Technol 2003;52:165–8.
[32] Natsu W, Ikeda T, Kunieda M. Generating complicated surface with electrolyte jet machining. Precision Eng 2007;31:33–9.
[33] Bilgi DS, Jain VK, Shekhar R, Mehrotra S. Electrochemical deep hole drilling in super alloy for turbine application. J Mater Process Technol 2004;149:445–52.
[34] Sen M, Shan HS. A review of electrochemical macro- to micro-hole drilling processes. I J Mach Tools Manuf 2005;45:137–52.
[35] Guodong L, Yong L, Quancun K, Hao T. Selection and optimization of electrolyte for micro electrochemical machining on stainless steel 304. Procedia CIRP 2016;42:412–7.
[36] Bhattacharyya B. Chapter 7 – influencing factors of EMM. In: Electrochemical micromachining for nanofabrication, MEMS and nanotechnology. 2015: William Andrew Publishing; 2017. p. 123–43.
[37] Rajurkar KP, Zhu D, McGeough JA, Kozak J, De Silva A. New developments in electro-Chemical machining. CIRP Ann Manuf Technol 1999;48:567–79.
[38] DeSilva AKM, Pajak PT, Harrison DK, McGeough JA. Modelling and experimental investigation of laser assisted jet electrochemical machining. CIRP Ann Manuf Technol 2004;53:179–82.
[39] Pajak PT, Desilva AKM, Harrison DK, McGeough JA. Precision and efficiency of laser assisted jet electrochemical machining. Precision Eng 2006;30:288–98.
[40] Jv Gutfeld R, Romankiw LT, Acosta RE. Laser-enhanced plating and etching: mechanisms and applications. IBM J Res Dev 1982;26:136–44.
[41] Datta M, Romankiw LT, Vigliotti DR, von Gutfeld RJ. Jet and laser-Jet electrochemical micromachining of nickel and steel. J Electrochem Soc 1989;136:2251–6.
[42] Liu Z, Nouraei H, Papini M, Spelt JK. Abrasive enhanced electrochemical slurry jet micro-machining: comparative experiments and synergistic effects. J Mater Process Technol 2014;214:1886–94.
[43] Liu Z, Nouraei H, Spelt JK, Papini M. Electrochemical slurry jet micromachining of tungsten carbide with a sodium chloride solution. Precision Eng 2015;40:189–98.
[44] Kock M, Kirchner V, Schuster R. Electrochemical micromachining with ultrashort voltage pulses–a versatile method with lithographical precision. Electrochim Acta 2003;48:3213–9.
[45] Kozak J, Gulbinowicz D, Gulbinowicz Z. The mathematical modeling and computer simulation of pulse electrochemical micromachining. Eng Lett 2008;16:556–61.
[46] Yu YQ, Zhao JS, Li BH, Xu JW. Experimental study of pulsed electrolyte jet machining for small hole. Key Eng Mater 2010;458:307–12.
[47] Kawanaka T, Kunieda M. Mirror-like finishing by electrolyte jet machining. CIRP Ann Manuf Technol 2015;64:237–40.
[48] Lange NA. Lange's handbook of chemistry. 15th ed. New York: McGraw-Hill; 1999.